CONDENSED MATTER PHYSICS

Floquet metal-to-insulator phase transitions in semiconductor nanowires

Iliya Esin[1]*, Mark S. Rudner[2], Netanel H. Lindner[1]

We study steady states of semiconductor nanowires subjected to strong resonant time-periodic drives. The steady states arise from the balance between electron-phonon scattering, electron-hole recombination via photoemission, and Auger scattering processes. We show that tuning the strength of the driving field drives a transition between an electron-hole metal (EHM) phase and a Floquet insulator (FI) phase. We study the critical point controlling this transition. The EHM-to-FI transition can be observed by monitoring the presence of peaks in the density-density response function, which are associated with the Fermi momentum of the EHM phase and are absent in the FI phase. Our results may help guide future studies toward inducing exotic nonequilibrium phases of matter by periodic driving.

INTRODUCTION

Coherent time-periodic driving provides a versatile tool for inducing novel properties in solid state and atomic systems (*1*–*12*). Prominent applications include Floquet engineering of band topology, light-induced superconductivity, and ultrafast spintronics (*13*–*29*). In many contexts, interesting phenomena may be observed in the short-time dynamics of driven systems (*30*–*32*). Under appropriate conditions, at long times, Floquet systems may also exhibit nontrivial steady-state characteristics such as topological responses or time-crystalline behavior (*33*–*47*).

Here, we investigate transitions between distinct phases realized in the steady states of a periodically driven semiconductor nanowire. We study the case where the drive frequency is larger than the band gap of the material. For weak (incoherent) driving, the steady state is established by a competition between excitation and relaxation rates that lead to a population inversion (i.e., the steady state hosts a nonequilibrium density of excited electrons at the bottom of the conduction band and holes at the top of the valence band, as indicated in Fig. 1A) (*48*, *49*).

When the drive is sufficiently strong, the conduction and valence bands are coherently hybridized for momenta near the "resonance momenta" $\pm k_R$ (see Fig. 1B). In this situation, the Floquet bands provide a good basis for identifying the physical properties and response characteristics of the many-body steady state. Here, we study such strongly driven systems, in the regime where the steady state is well described in terms of electronic populations of the system's Floquet-Bloch states, with a nearly insulator-like filling in the Floquet basis. Such a system serves as a prototype for a Floquet topological insulator in which a resonant drive is used to induce an effective band inversion (*19*, *46*, *50*, *51*).

An ideal Floquet insulator (FI) is characterized by having a set of Floquet bands that are fully filled, while the remaining Floquet bands are empty. Away from the resonance momenta, the band inversion featured by the ideal FI implies that it hosts a nonequilibrium density of electrons and holes in the conduction and valence bands of the system's equilibrium band structure. In this respect, the steady state bears similarity to that of a weakly driven system as shown in Fig. 1A. The natural relaxation of these electrons and holes through radiative recombination is manifested in the Floquet picture as interband transitions that create excitations away from the ideal FI state (making holes in the nominally filled Floquet band and putting electrons into the nominally empty Floquet band). Spontaneous emission therefore contributes a source of "quantum heating" in the Floquet basis (see Fig. 1B, wiggly arrow) (*52*). Similarly, inter-Floquet band transitions arising from electron-electron interactions may also create excitations away from the ideal FI state. At the same time, spontaneous electron-phonon scattering may lead to interband transitions that reduce the number of excitations, helping to "cool" the system toward the FI state (Fig. 1B, straight arrows). The steady state is determined by the competition between these scattering processes.

The steady states of nonequilibrium systems are generally sensitive to the rates of scattering processes, which, in turn, depend on a large number of microscopic parameters of the system and the baths to which it is coupled (in contrast to equilibrium where statistical mechanics provide a simple description of steady states in terms of a small number of thermodynamic parameters such as chemical potential and temperature). Nevertheless, we show that the electronic steady states of resonantly driven semiconductor nanowires exhibit two phases, distinguished by their properties for momenta near the resonance: (i) an electron-hole metal (EHM) phase, which features sharp Fermi surfaces for electron and hole excitations in the nominally empty and filled Floquet bands, respectively, and (ii) an FI phase, in which the electron and hole excitations are distributed as a nondegenerate Fermi gas in the Floquet basis. Which of these phases is obtained is determined by the dependence of the inter-Floquet band relaxation rates on the excitation density. A bottleneck for relaxation arises in the situation where these relaxation rates are suppressed at low densities, leading to a pileup of excitations and the formation of an EHM.

We show that a simple phase diagram emerges that is controlled by just two effective parameters, which capture the competition between the processes described above. The structure of the phase diagram is governed by a quantum critical point, with a critical region separating the two phases (see Fig. 1C). The transition between the EHM and the FI across the critical region is reminiscent of a finite-temperature crossover. The properties of the crossover are determined by the effective temperature of the electron and hole excitations in the Floquet bands.

[1]Physics Department, Technion, 3200003 Haifa, Israel. [2]Center for Quantum Devices and Niels Bohr International Academy, Niels Bohr Institute, University of Copenhagen, 2100 Copenhagen, Denmark.
*Corresponding author. Email: iliyaesin@campus.technion.ac.il

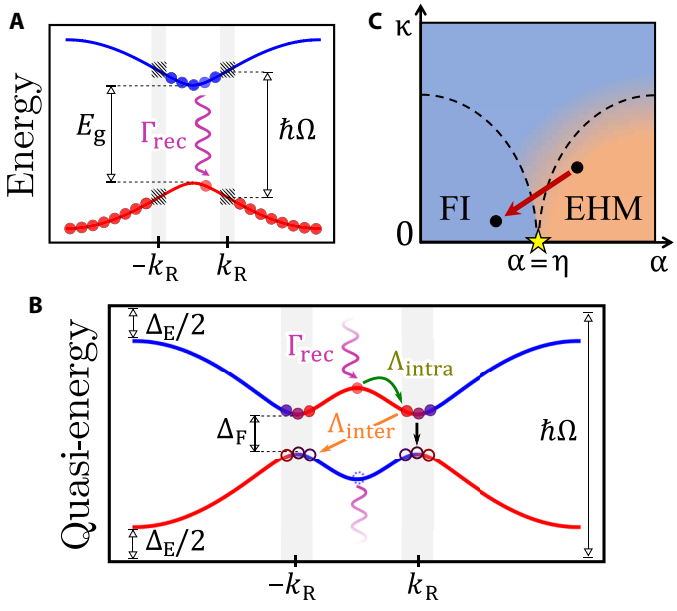

Fig. 1. Scattering processes underlying the steady state and the resulting phase diagram. (**A**) Equilibrium band structure of the semiconductor nanowire. Full circles represent an average occupation of the conduction and valence bands exhibiting a photon-excited population induced by the driving field. Wiggly line represents radiative recombination processes. The periodic drive is resonant at the momenta $\pm k_R$. The states near the resonance momenta (indicated by hatched boxes) are strongly coherently hybridized and therefore should be analyzed in terms of electronic populations in the Floquet bands. (**B**) Floquet spectrum of the periodically driven system described by the model in Eq. 1. The wiggly arrow indicates photon-mediated Floquet Umklapp excitations, identical to the radiative recombination processes shown in (A). Phonon-mediated inter-Floquet band scattering processes are indicated by black and orange straight arrows, corresponding to intravalley and intervalley scattering, respectively. The corresponding rates become suppressed at low densities according to characteristic power laws (see, for example, Eq. 10 and surrounding text). We capture the net suppression power law using an effective bottleneck parameter α. The green curved arrow indicates phonon-mediated intraband relaxation. (**C**) Phase diagram of the steady state as a function of α and the parameter κ, which captures the ratio of the intrinsic rates of heating and cooling processes (in the Floquet basis) (see Eq. 8). The system exhibits a quantum phase transition at $\kappa \to 0$ and $\alpha = \eta$, where η is the exponent appearing in the ω dependence in the phonon density of states (Eq. 5). For $\kappa > 0$, the phase transition becomes a crossover, separating an EHM featuring sharp Fermi surfaces for excitations in the Floquet bands from an FI with a low-density nondegenerate gas of excitations. Red arrow indicates the EHM-to-FI transition induced by increasing drive strength, which changes the effective value of α.

As explained above, our main goal is to identify the important parameters that control the phase diagram and to characterize the critical point that separates the EHM and FI phases. To this end, we develop a simple analytical model based on a rate equation approach that captures the key mechanisms that determine the steady state of the driven system. For concreteness, we begin by providing a fully specified model for the driven system and the coupling to the environment. After obtaining the analytical results, we use numerical simulations of this microscopic model to verify the phase diagram and scaling behavior predicted by the rate equation approach. Last, we show that the phase diagram can be explored by tuning the driving frequency and strength. We further show that the EHM phase can be experimentally identified by observing peaks in the density-density response associated with the Fermi momentum of the excited electrons. This response gives rise to Friedel oscillations in the density induced by local inhomogeneities or an external potential.

RESULTS

Model of a periodically driven nanowire

To study the EHM and FI phases, we use a tight-binding model describing a uniformly, periodically driven nanowire with the Hamiltonian $\hat{\mathcal{H}}_0(t) = \sum_k \hat{\boldsymbol{c}}_k^\dagger H_k(t)\,\hat{\boldsymbol{c}}_k$. Here, $\hat{\boldsymbol{c}}_k = (\hat{c}_{\mathcal{A},k}\ \hat{c}_{\mathcal{B},k})^{\mathrm{T}}$ is a vector of operators annihilating spinless fermions in two orbitals, $|\mathcal{A}\rangle$ and $|\mathcal{B}\rangle$, with crystal momentum k along the wire. We write the single-particle Bloch Hamiltonian $H_k(t)$ in the form (*53*–*57*)

$$H_k(t) = [M - B\cos(ka)]\,\sigma^z + A\sin(ka)\,\sigma^y + V\cos(\Omega t)\,\sigma^x \quad (1)$$

where σ^x, σ^y, and σ^z are Pauli matrices in the orbital basis, with $\sigma^z|\mathcal{A}\rangle = |\mathcal{A}\rangle$ and $\sigma^z|\mathcal{B}\rangle = -|\mathcal{B}\rangle$, and A, B, and M are constants. The periodic drive induces a local coupling between the orbitals, with strength V. Throughout this work, we consider a half-filled system, which is a band insulator in the absence of the drive. The Floquet eigenstates of the time-dependent problem satisfy $\left[i\hbar\frac{\partial}{\partial t} - H_k(t)\right]|\psi_{k\nu}(t)\rangle = 0$, with $|\psi_{k\nu}(t)\rangle = e^{-i\varepsilon_{k\nu}t/\hbar}|\phi_{k\nu}(t)\rangle$. Here, $|\phi_{k\nu}(t)\rangle = \sum_m e^{-im\Omega t}|\phi_{k\nu}^m\rangle$ is time periodic with period $\mathcal{T} = 2\pi/\Omega$, and $\varepsilon_{k\nu}$ is the quasi-energy. Throughout, we use the convention $-\hbar\Omega/2 \le \varepsilon_{k\nu} < \hbar\Omega/2$.

We study the regime where $2\hbar\Omega$ is less than the total bandwidth $(2|M| + 2|B|)$. In this regime, the drive only resonantly couples states in the two bands via single-photon resonances; these resonances occur at crystal momentum values $k = \pm k_R$, where $\hbar\Omega$ matches the splitting between valence and conduction bands of the nondriven system. The resulting Floquet spectrum exhibits a gap, Δ_F, separating the upper ($\nu = +$) and lower ($\nu = -$) Floquet bands. The form of the drive that appears in Eq. 1 is chosen such that the magnitude of the gap is equal to the driving field strength, up to corrections of order $V^2/\hbar\Omega$. Other forms of the drive, such as a linearly polarized electric field, would have a different relation between the drive amplitude and Δ_F and would yield qualitatively similar results. A plot of a generic quasi-energy band structure for the Hamiltonian in Eq. 1 is shown in Fig. 1B.

System-bath coupling

In addition to the coherent effects of the drive, captured in Eq. 1, we also describe the key dissipative processes that govern the steady states of the system. To this end, we incorporate in the model couplings between the electrons of the nanowire and acoustic phonons of the d-dimensional substrate upon which it sits (with $d \ge 2$), as well as coupling of the electronic system to its (three-dimensional) electromagnetic environment. For simplicity, we consider a single-polarization mode for each bosonic bath (phonons or photons). The electromagnetic coupling allows radiative recombination of electron-hole pairs via spontaneous photon emission, which provides the primary source of heating in the Floquet basis. The effect of electron-electron interactions on the steady state is discussed in section S1.

The electron-boson coupling Hamiltonian $\hat{\mathcal{H}}_\lambda^{e-b}$ (used for both photons, $\lambda = \ell$ for "light," and phonons, $\lambda = s$ for "sound") reads

$$\hat{\mathcal{H}}_\lambda^{e-b} = \sum_{k,\mathbf{q}} \hat{\boldsymbol{c}}_k^\dagger U_\lambda(q,\omega)\,\hat{\boldsymbol{c}}_{k+q}\,\hat{b}_{\lambda,\mathbf{q}}^\dagger + \mathrm{h.c.} \quad (2)$$

Here, $\hat{b}_{\lambda,\mathbf{q}}$ annihilates a photon (for $\lambda = \ell$) or an acoustic phonon (for $\lambda = s$), with crystal momentum $\mathbf{q} = (q, \mathbf{q}_\perp)$, and frequency $\omega = v_\lambda |\mathbf{q}|$, where v_λ is the speed of light or sound. The Hamiltonian describing the heat baths reads $\hat{\mathcal{H}}_\lambda = \sum_{\mathbf{q}} \hbar v_\lambda |\mathbf{q}| \hat{b}^\dagger_{\lambda,\mathbf{q}} \hat{b}_{\lambda,\mathbf{q}}$. The first component of $\mathbf{q}$, denoted q, is the crystal momentum component parallel to the wire, and $q_\perp$ represents its orthogonal component(s). (For photons, $q_\perp$ has two components, while for phonons, $q_\perp$ has one or two components, depending on whether $d = 2$ or $d = 3$.) The microscopic details of the electron-photon and electron-phonon couplings are captured by the functions $U_\lambda(q, \omega)$.

Respecting the particle-hole symmetry of the system, for small q, we take the coupling between electrons and acoustic phonons polarized along the wire to be (*57*, *58*)

$$U_s(q,\omega) = u_s q + \mathcal{O}(q^2);\ u_s(\omega) \equiv g_s \sqrt{a v_s/\omega} \tag{3}$$

Here, g_s is a coupling parameter, and U_s is proportional to the unity matrix in the $\mathcal{A}$, $\mathcal{B}$ orbital space. For the electron-photon coupling, we take the simple ($\mathbf{q}$ independent) form $U_\ell = g_\ell \sigma^x$, where g_ℓ is a coupling parameter and σ^x is an orbital-space Pauli matrix (see text below Eq. 1). Our results can easily be extended to describe systems with other forms of electron-phonon coupling.

Floquet kinetic equations

We work in the regime of weak system-bath coupling, where close to the steady state the electronic density matrix is well described in terms of populations of the Floquet eigenstates (*14*, *46*, *50*). Specifically, we will consider the regime $\hbar W_{\mathrm{scat}} \ll \Delta_F$, where W_{scat} is a typical scattering rate for an electron in the steady state (*50*). These populations are given by $f_{k\nu}(t) = \langle \hat{\phi}^\dagger_{k\nu}(t) \hat{\phi}_{k\nu}(t) \rangle$, where $\hat{\phi}^\dagger_{k\nu}(t)$ creates an electron in the Floquet state $e^{-i\epsilon_{k\nu} t} |\phi_{k\nu}(t)\rangle$.

The system-bath coupling induces transitions between Floquet states. As a result, the populations $\{f_{k\nu}\}$ evolve according to the kinetic equation

$$\dot{f}_{k\nu}(t) = \sum_{k'\nu'\lambda} [I_\lambda(k'\nu', k\nu) - I_\lambda(k\nu, k'\nu')] \tag{4}$$

where $I_\lambda(k\nu, k'\nu') = \sum_l W^{(l)}_\lambda(k\nu, k'\nu') f_{k\nu}(1 - f_{k'\nu'})$ describes the rate of electron transitions from state k in Floquet band ν to state k' in Floquet band ν'. For a zero temperature bath, the intrinsic rate $W^{(l)}_\lambda(k\nu, k'\nu')$ describes the corresponding scattering rate for a single electron in an otherwise empty system, involving spontaneous emission of a bath boson (phonon or photon) with energy $\hbar\omega_l = \epsilon_{k\nu} - \epsilon_{k'\nu'} - l\hbar\Omega$ (see Eq. 16).

Because of the large speed of light, the momentum transfer $q = k - k'$ associated with spontaneous photon emission is small: $|q| \ll \omega/v_\ell$. We thus take the density of states of the photon reservoir, integrated over perpendicular momentum components, as $\rho_\ell(q,\omega) = \rho^0_\ell \cdot a\omega/v_\ell$ when $\omega > v_\ell |q|$ and $\rho_\ell(q, \omega) = 0$ otherwise. Here, ρ^0_ℓ is constant, independent of q and ω.

Similarly, allowing substrates of different dimensionality, the phonon density of states reads

$$\rho_s(\omega) = \rho^0_s \cdot (a\omega/v_s)^\eta \tag{5}$$

when $v_s |q| < \omega < \omega_D$ and $\rho_s(q, \omega) = 0$ otherwise. For acoustic phonons in a d-dimensional homogeneous substrate, $\eta = d - 2$. The value of η also depends on the dispersion of phonons. Here, ρ^0_s is a constant.

Note that $\rho_s(q, \omega)$ is cut off at the Debye frequency, ω_D. Throughout this work, take ω_D to be in the range $\Delta_F < \hbar\omega_D < \Delta_E$, where Δ_E is the gap at the quasi-energy zone edge $\epsilon = \hbar\Omega/2$ (see Fig. 1B). The condition $\hbar\omega_D < \Delta_E$ ensures the absence of phonon-mediated Floquet-Umklapp processes, corresponding to transitions with $l > 0$ (see text below Eq. 4) (*50*).

Analysis of the steady state

We now analyze the steady state that emerges from the interplay between "excitation" processes associated with spontaneous emission of photons and "relaxation" processes mediated by the emission of acoustic phonons. From this analysis, we will extract the two key parameters that control the phase diagram of the system and characterize the critical point that separates the EHM and FI phases.

In the steady state, most of the excited electrons pile up in the two "valleys" near the minima of the upper Floquet band [see Fig. 1B and (*50*)]. The pileup results from a bottleneck in the excitation-relaxation cycle. This bottleneck is due to small intrinsic rates of inter-Floquet band relaxation for electrons close to the band minima compared with the rates of phonon-mediated intra-Floquet band relaxation of highly excited electrons within the upper Floquet band (see detailed discussion below). Because of particle-hole symmetry in our model, the holes form a mirror image population in the lower Floquet band.

Within the regime of interest, the distributions of electrons near the bottom of the upper Floquet band (f_{k+}) and holes near the top of the lower Floquet band ($1 - f_{k-}$) can, to a good degree, be approximately described by separate Fermi-Dirac distributions related by $f_{k+} = 1 - f_{k-}$, where

$$f_{k+} = [1 + e^{(\epsilon_{k+} - \mu)/T}]^{-1} \tag{6}$$

This assertion will be verified by our numerical simulations below. Here, μ and T are the effective chemical potential counted from the bottom of the band and temperature of the electrons in the upper Floquet band (in energy units, $k_B = 1$, where k_B is Boltzmann's constant). We note that although most of the excitations occupy the band minima according to Eq. 6, a small but finite density of excitations occupying high quasi-energy levels is necessary to maintain this distribution.

The EHM and FI phases are distinguished by whether μ lies above the bottom of the upper Floquet band, giving rise to a sharp Fermi surface for $\mu \gg T$ (EHM phase), or below the band (i.e., in the Floquet gap), giving the FI phase. We thus seek to characterize the dependence of μ and T on the parameters of the system and the heat baths. To this end, we first develop a phenomenological model that captures the phase structure of the system and allows us to extract these dependencies. We will then corroborate these predictions with numerical simulations of the full kinetic equation (Eq. 4). In the main text, our analysis is done for zero bath temperature. The effects of finite bath temperature are discussed in section S2.

Balance equation for the excitation density

To build the phenomenological model, we seek two balance equations that must be satisfied by the populations of the Floquet bands in the steady state. The first balance equation fixes the value of

the total excitation density of electrons in the upper Floquet band, $n = \int_{-\pi/a}^{\pi/a} \frac{dk}{2\pi} f_k$. For simplicity, we suppress the band index on the population and define $f_k \equiv f_{k+}$. The equation for n describes the balance between interband excitation and relaxation processes (*48*, *49*). A given value of n corresponds to many different combinations of μ and T. A second equation, following from the balance of intraband and interband relaxation processes, provides the relation between μ and T.

We now analyze the processes leading to the steady state in more detail. Electron-hole excitations are predominantly generated by photon-mediated Floquet-Umklapp processes. In the low-excitation regime, $na \ll 1$, which we consider throughout, photon-mediated processes excite electrons from an almost full to an almost empty Floquet band. Therefore, the excitation rate $\dot{n}|_{\text{rec}} = \Gamma_{\text{rec}}$ is approximately independent of the steady-state distribution. Once excited, electron excitations quickly relax into the valleys of the upper Floquet band near $k = \pm k_R$ and accumulate there. A mirror image process applies for the holes.

Annihilation of Floquet electron-hole pairs, which is primarily mediated by phonons, occurs on longer time scales than the relaxation to the band minima. The rate of such processes is proportional to the density of electron excitations in the upper Floquet band and hole excitations in the lower Floquet band, i.e., $\dot{n}|_{\text{inter}} = -\Lambda_{\text{inter}} n^2$ (*50*) (here, we used that the electron and hole densities are equal for half filling). The rate equation for the density of excited electrons due to inter- and intra-Floquet band processes thus reads

$$\dot{n} = \Gamma_{\text{rec}} - \Lambda_{\text{inter}} n^2 \tag{7}$$

The steady-state solution is obtained upon setting $\dot{n} = 0$, which yields

$$n = \kappa^{\frac{1}{2}} \; ; \kappa \equiv \Gamma_{\text{rec}}/\Lambda_{\text{inter}} \tag{8}$$

Here, κ is the "balance parameter," denoting the balance between photon-mediated heating and phonon-mediated cooling processes. κ depends on the system parameters and, in particular, on the forms and strengths of the electron-phonon and electron-photon coupling. When $\kappa = 0$, the steady state resembles a zero-temperature Gibbs distribution in terms of the Floquet quasi-energies (*59*).

Balance equations for μ and T

Next, we split the excitations in the upper band into two subpopulations of high and low quasi-energy excitations, which will allow us to characterize the form of the distribution (i.e., to determine μ and T). We partition the Brillouin zone into a momentum sector of width $2\Delta k$ around the minimum of the upper band, $\mathbb{K}_R = \{k | \; k_R - \Delta k < k < k_R + \Delta k\}$, and the complement of this sector. In the EHM phase, we choose Δk to be such that $f_{k_R \pm \Delta k} = \frac{1}{2}$; in the FI phase, we choose a small value of Δk with $\varepsilon_{k_R + \Delta k, +} - \varepsilon_{k_R, +} \ll T$ such that the distribution at $f_{k_R + \Delta k}$ can be approximated by f_{k_R}. The partition of the momentum domain yields the partition of the density in the upper band, n, into two contributions: n_R and δn, corresponding to the total density of electrons within $\mathbb{K}_R$, $n_R = 2\int_{\mathbb{K}_R} \frac{dk}{2\pi} f_k$, and all other excited electrons, $\delta n = n - n_R$ (see Fig. 2). The factor 2 in the definition of n_R accounts for the contributions of the two valleys.

The dominant source rate for n_R arises from the intraband scattering of electrons occupying quasi-energy states outside the region $\mathbb{K}_R$ into unoccupied states inside $\mathbb{K}_R$. Therefore, we estimate

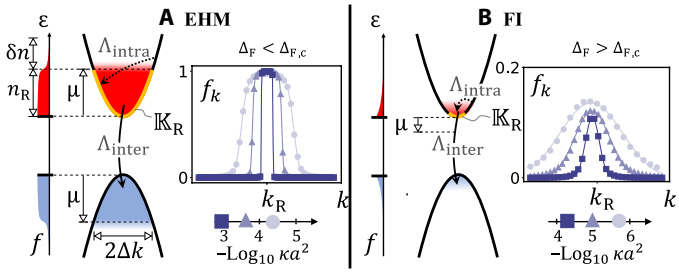

Fig. 2. Bottleneck effect. Relaxation processes leading to the steady state near the minimum and maximum of the Floquet bands. (**A**) In the EHM phase, the effective chemical potential μ for electrons (red), counted from the band bottom, is positive; the distribution of holes (blue) is related by particle-hole symmetry. Intraband relaxation (dotted arrow) predominantly occurs across the chemical potential, connecting states within the range of T around the chemical potential. Reducing the "bottleneck" parameter, α, causes the chemical potential, μ, to move toward zero, until it becomes negative at the critical value η, causing the transition toward the FI phase. (**B**) In the FI phase, the effective chemical potentials for the electrons and holes are negative, lying within the Floquet gap. Intraband relaxation processes (dotted arrow) collect excitations near the minima of the band. The orange-colored sectors in (A) and (B), labeled $\mathbb{K}_R$, indicate the states hosting the density n_R (see section "Balance equations for μ and T"). Insets to (A) and (B): Steady-state distributions near $k = k_R$ in the EHM and FI phases, respectively, for three values of the balance parameter, κ, indicated on the logarithmic scale below the insets. Data points show the steady-state distribution, and solid lines are the fits of the distribution to a shifted Fermi function. The transition between the EHM and FI phases in (A) and (B) was implemented by changing the drive amplitude from $V = 0.06\hbar\Omega$ to $V = 0.12\hbar\Omega$.

this rate by $\dot{n}_R|_{\text{intra}} = \Lambda_{\text{intra}} h_R \delta n$, where Λ_{intra} captures the average intrinsic rate of collisions across the boundary of $\mathbb{K}_R$, and $h_R \equiv \int_{\mathbb{K}_R} \frac{dk}{2\pi}(1 - f_k)$.

To estimate Λ_{intra}, we need to estimate the energy and momentum transferred between the electrons and the phonons in this scattering process. We first note that as f_k decays over a quasi-energy window of order T, we expect the densities δn and h_R to be mostly concentrated in this window. Therefore, we estimate the energy of the phonons emitted in the processes contributing to $\dot{n}_R|_{\text{intra}}$ as $\hbar\omega \sim T$. The density of states for such phonons is nonvanishing for momentum transfers $|q| < T/\hbar v_s$. Therefore, large momentum-transfer intraband processes connecting populations in the valleys near k_R and $-k_R$ are forbidden for low-temperature steady states, which satisfy $T < 2k_R\hbar v_s$.

Because of the momentum dependence of $U_s(q, \omega)$ (Eqs. 2 and 3), the main contributions to Λ_{intra} come from the largest momentum transfers allowed within each valley, which we label q_*. Because at low densities q_* is small on the characteristic momentum scale of the Floquet dispersion, the overlap of the states before and after the transition is almost 1. Thus, we evaluate the electron-phonon coupling matrix element between these states by $q_* u_s(\omega)$ (see Eq. 3). Using Floquet-Fermi's golden rule (see Eq. 16), we estimate

$$\Lambda_{\text{intra}} \propto q_*^2 u_s^2(T) \rho_s(T) \tag{9}$$

The source rate for n_R is balanced by annihilation of electrons comprising the population n_R with holes in the lower Floquet band, accompanied by phonon emission. These inter-Floquet band relaxation processes act as a sink for the density of excitations; the total rate of these depletion processes is proportional to the population

and the total density of holes in the lower Floquet band, which is given by n. We thus estimate $\dot{n}_R|_{inter} = -\Lambda_{inter} n_R n$.

The net interband scattering rate has two main contributions. The first arises from "vertical" (intravalley) processes (shown by a black arrow in Fig. 1B) and the second from "diagonal" (intervalley) processes (shown by an orange arrow). The former (intravalley) processes involve small momentum transfers, $q \lesssim q_*$, while the latter processes require large momentum transfers, $q \approx 2k_R$, where $2k_R$ is the separation in momentum of the two valleys. In both cases, the energy of the emitted phonon is approximately equal to the Floquet gap, $\hbar\omega \approx \Delta_F$. The intervalley processes are therefore kinematically constrained due to the large momentum transfers involved and only become active when the Floquet gap is above a critical value $\Delta_{F,c} \equiv 2\hbar v_s k_R$.

As a first step, we consider the case where the drive strength is low enough that the Floquet gap is below the critical value, $\Delta_F < \Delta_{F,c}$, where only the intravalley phonon-mediated inter-Floquet band scattering processes are active. To evaluate Λ_{inter}, we must estimate the electron-phonon matrix element governing these processes. We note that such processes connect nearly orthogonal electronic states (in different bands, at nearby momenta). Given the matrix form of the electron-phonon coupling in Eq. 3, for small q, the matrix element of the intravalley process is proportional to $q^2 u_s(\Delta_F)$. In this estimate, we have used that the energy transfer is approximately equal to the Floquet gap, Δ_F.

Because of the fact that the matrix element above is suppressed for small q, the intravalley interband transition rate will be dominated by processes with the maximal momentum transfer, q_*. Thus, from Fermi's golden rule, we obtain

$$\Lambda_{inter} \propto q_*^{2\alpha} u_s^2(\Delta_F)\, \rho_s(\Delta_F) \tag{10}$$

where $\rho_s(\Delta_F)$ is the phonon density of states (Eq. 5) evaluated at the energy transfer Δ_F. Here, we have defined α to highlight the total power of q_*^2 appearing in the expression for Λ_{inter} in Eq. 10. Our model, Eq. 1, gives $\alpha = 2$. Below, we will discuss the relation between q_* and the excitation density in each phase. Through this relation, we will see that α characterizes how the interband transition rate is suppressed at small excitation density. We thus refer to α as the "bottleneck parameter," as it controls the ratio $\Lambda_{inter}/\Lambda_{intra}$.

Combining all of the source and sink rates for n_R found above, we arrive at the rate equation

$$\dot{n}_R = \Lambda_{intra} h_R \delta n - \Lambda_{inter} n_R n \tag{11}$$

Below, we will use Eq. 11, together with Eq. 8, to analyze the properties of the EHM and FI phases.

Before turning to the analysis of the two phases, we note that for the specific model and regime discussed so far, the bottleneck parameter takes the value $\alpha = 2$. However, the rate equation analysis applies more broadly, when α takes other values. In particular, we note that the initial and final electronic states of the intervalley interband scattering processes typically do not suffer from the near-orthogonality discussed for the intravalley processes. Moreover, for these processes, the electron-phonon coupling $U_s(q, \omega)$ is evaluated at a momentum transfer $q \sim 2k_R$. Hence, the rates of intervalley interband scattering processes are governed by $\Lambda'_{inter} \propto (2k_R)^2 u_s^2(\Delta_F)\, \rho_s(\Delta_F)$. Because there is no small momentum q_* appearing in Λ'_{inter}, according to the definition of α in Eq. 10, a system dominated by intervalley interband scattering would be described by $\alpha = 0$. Therefore, in the analysis below, we will use α as an effective parameter to capture the net suppression of the inter-Floquet band relaxation rate at low densities. The effective value of α depends on the parameters of the system (such as the form of the electron-phonon coupling) and can be controlled in situ by the drive strength, as will be discussed below. Another important parameter controlling the behavior of the system is the exponent η in the phonon density of states (Eq. 5).

Below, we treat α and η as free parameters and map out a phase diagram (Fig. 1C) that captures the behavior across different parameter regimes (with a transition controlled by $\alpha - \eta$). In particular, we will demonstrate the existence of a phase transition between the EHM and FI phases by obtaining critical exponents that characterize the phase transition in terms of α and η.

The EHM phase

We begin by considering the situation when interband relaxation is the rate-limiting step in the relaxation cascade of excited Floquet electron-hole pairs. This regime realizes the EHM phase, where the excitations on top of the FI state exhibit sharp Fermi surfaces, $\mu \gg T$. We will use Eqs. 8 to 11 to obtain the conditions on α and η where this regime is realized.

We now use Eq. 11 to obtain a relation between μ and T in the steady state (when $\dot{n}_R = 0$). To this end, we express Λ_{inter} and Λ_{intra} by their estimates as functions of q_* and T, respectively (Eqs. 9 and 10). Under the assumption $\mu \gg T$, we have that f_k equals $\frac{1}{2}$ at quasienergy $\varepsilon = \mu$. From the definition of $\mathbb{K}_R$, the momentum window defining the population n_R, this yields $\Delta k = \pi n/2$. We evaluate the densities $n \approx n_R \approx 4\mu D(\mu)$ and $\delta n \approx h_R \approx 2TD(\mu)$, where $D(\varepsilon)$ is the electronic density of states near the parabolic minimum of the upper Floquet band. Using this in Eq. 11 and solving for the steady state gives $(2\mu/T)^2 = \Lambda_{intra}/\Lambda_{inter}$. Next, we evaluate the maximal momentum transfer as $q_* \approx \pi n$. Using $D(\varepsilon) \approx D_0\sqrt{\Delta_F/\varepsilon}$, where D_0 is a constant, and $\rho_s \sim \omega^\eta$ (see Eq. 5), we obtain

$$\mu/T = c(T/\Delta_F)^{\frac{\eta-\alpha}{\alpha+1}} \tag{12}$$

where c is a numerical constant of the order of unity.

By definition, the existence of an EHM phase with a sharp Fermi surface and a small density of excitations requires $\mu/T \gg 1$ and $T/\Delta_F \ll 1$. In order for the relation in Eq. 12 to be satisfied along with these conditions in the limit of small effective temperatures, the exponent $(\eta - \alpha)/(\alpha + 1)$ must be negative; therefore, the EHM phase requires $\alpha < \eta$. Again, using $n \approx 4\mu D(\mu)$ and expressing n in terms of κ as in Eq. 8, Eq. 12 yields relations for T and μ in terms of

$$T/\Delta_F \sim (\kappa/\kappa_0)^{\nu_T};\ \mu/\Delta_F \sim (\kappa/\kappa_0)^{\nu_\mu} \tag{13}$$

where $\kappa_0 = (\Delta_F D_0)^2$. Explicit expressions for ν_T and ν_μ appear in the table in Fig. 3A.

Another characteristic feature of the EHM phase is the dependence of the excitation density on the recombination rate Γ_{rec} (with all other parameters fixed). Taking into account the implicit dependence of Λ_{inter} on the excitation density through Eq. 10, from Eq. 8 we find $n \propto \Gamma_{rec}^{\frac{1}{2\alpha+2}}$.

The FI phase

As explained below Eq. 12, for $\alpha < \eta$, the EHM is not a consistent steady state of the rate Eqs. 7 and 11. We will now analyze the rate

	EHM ($\alpha > \eta$)	FI ($\alpha < \eta$)
ν_T	$\frac{\alpha+1}{\eta+1}$	$\frac{1}{2\eta-2\alpha+1}$
ν_μ	1	–
ν_z	–	$\frac{\eta-\alpha}{2\eta-2\alpha+1}$

A

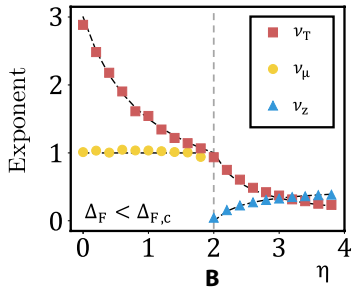

B

Fig. 3. Scaling exponents in the EHM and FI phases. (**A**) Analytic prediction from the phenomenological model for the exponents of effective temperature, $T/\Delta_F \sim (\kappa/\kappa_0)^{\nu_T}$, effective chemical potential, $\mu/\Delta_F \sim (\kappa/\kappa_0)^{\nu_\mu}$, and the fugacity, $z \sim (\kappa/\kappa_0)^{\nu_z}$, in the EHM and FI phases. (**B**) Numerical results of the scaling exponents ν_T, ν_μ, and ν_z obtained from fits of steady-state distributions, obtained by solving the full kinetic Eq. 4, to the Fermi function, Eq. 6. In the simulation, we fix $\Delta_F < \Delta_{F,c}$ (which sets $\alpha = 2$) and vary the parameter η, which controls the phonon density of states (see Eq. 5). Black dashed lines correspond to analytic predictions in (A); gray dashed line denotes the EHM-to-FI phase transition point at $\eta = \alpha$. The nonanalytic behavior of the exponents at this point implies the existence of a quantum critical point when $\kappa \to 0$ (see Fig. 1C).

Eqs. 7 and 11 assuming that the distribution is a nondegenerate Fermi gas with $\mu < 0$ (i.e., the chemical potential lies within the Floquet gap, below the band), which is characteristic of the FI phase. We will show that this distribution is a consistent solution of the rate Eqs. 7 and 11 for $\alpha < \eta$.

We approximate the distribution as $f_k \approx ze^{-\epsilon_{k+}/T}$, where $z = e^{-|\mu|/T}$ is the fugacity. Our target here is to characterize the FI phase by solving for z, which gives the occupation at the bottom of the upper Floquet band and is related to the excitation density via $n \approx 2\sqrt{\pi}zD(T)T$. Assuming $z \ll 1$, we fix the value of Δk in the definition of $\mathbb{K}_R$ such that $\Delta k \ll D(T)T$ (see Fig. 2B). We note that other choices of Δk will lead to the same power-law dependence. For this choice of Δk, f_k is approximately constant within the region $\mathbb{K}_R$, and we thus approximate $n_R \approx 4z\Delta k$, $h_R \approx 4\Delta k$, and $\delta n = n - n_R \approx n$. Substituting these relations into Eq. 11 gives $z = \Lambda_{intra}/\Lambda_{inter}$.

The spread of the density δn over the momentum domain determines the typical momentum transfer, $q_* \approx TD(T)$. Given this value of q_* in the definitions of Λ_{intra} and Λ_{inter} (Eqs. 9 and 10), we solve for the steady state of Eq. 11, $\dot{n}_R = 0$, to obtain

$$z = c'(T/\Delta_F)^{\eta-\alpha} \tag{14}$$

Here, c' is a numerical coefficient of order unity, generically different from c in Eq. 12.

Combining Eq. 14 with the expressions $n \approx 2\sqrt{\pi}\,zD(T)\,T$ and $n \approx \kappa^{1/2}$ yields a dependence of z and T on κ for the FI phase in the form of power laws with exponents ν_T and ν_z

$$T/\Delta_F \sim (\kappa/\kappa_0)^{\nu_T},\ z \sim (\kappa/\kappa_0)^{\nu_z} \tag{15}$$

The exponents are summarized in the table in Fig. 3A.

Another characteristic feature of the EHM phase is the dependence of the excitation density on the recombination rate Γ_{rec} (with all other parameters fixed). Taking into account the implicit dependence of Λ_{inter} on the excitation density through Eq. 10, from Eq. 8 we find $n \propto \Gamma_{rec}^{(\eta-\alpha+1/2)/(2\eta-\alpha+1)}$.

Note the difference between the exponents ν_T in the FI and EHM phases. This difference, together with the power laws for z in the FI phase and μ in the EHM phase, indicate discontinuous dependencies of these quantities on κ (at small κ). This nonanalytic behavior implies the existence of a quantum critical point at $\alpha = \eta$ when $\kappa \to 0$. Increasing κ increases the effective temperature of the steady state, T, giving rise to a finite effective temperature crossover above the critical point in the $\kappa - \alpha$ plane. The phase diagram (in the $\kappa - \alpha$ plane) characterizing the steady state of the system is depicted in Fig. 1C.

Numerical results

To support the analysis above, we numerically solve for the steady state of the full Floquet kinetic equation (Eq. 4) on a lattice of 5000 k points at half filling. Because the effective value of α depends in a complicated way on the system and drive parameters, in the numerical simulations, we verified the critical behavior near the EHM-to-FI phase transition by fixing α and varying η. We fixed $\alpha = 2$ by setting $\Delta_F < \Delta_{F,c}$ and swept the value of η (see Eq. 5) from $\eta = 0$ to $\eta = 4$ across the critical value at $\eta = \alpha = 2$. For each fixed set of parameters, we fit the steady-state distribution of electrons in the upper Floquet band to a Fermi-Dirac distribution (Eq. 6) to extract T, μ, and z. We repeat this procedure for several values of g_ℓ and a fixed g_s, yielding values of κ over several decades, and extract the power-law scalings of these three quantities as functions of κ. The resulting numerically extracted exponents ν_T, ν_μ, and ν_z are plotted as functions of η in Fig. 3B. We find good agreement between our analytical and numerical results.

Inducing and observing the phase transition

In this section, we discuss how to induce and observe the transition between the EHM and FI phase in a system with fixed band structure and bath parameters. By tuning the driving amplitude, which controls the Floquet gap Δ_F, the kinematic constraints that control the relative contributions of intravalley and intervalley interband scattering processes can be modified in situ. So far, we discussed the regime $\Delta_F < \Delta_{F,c}$, in which only the intravalley processes, corresponding to $\alpha = 2$, are active (see the discussion above Eq. 10). For $\Delta_F > \Delta_{F,c}$, however, the kinematic constraint on the phonons that forbids the intervalley processes is lifted. In this case, the interband relaxation rate consists of a sum of the intravalley and intervalley processes (see Fig. 1B).

As discussed above, the intervalley interband relaxation processes are generically characterized by $\alpha = 0$. In the presence of both processes, we expect an intermediate behavior between that described by the power laws in Eqs. 13 and 15 with $\alpha = 2$ and $\alpha = 0$. However, for small values of κ, processes with the lowest value of α dominate. Therefore, for $\eta = 1$, corresponding to phonons in three dimensions, the system should undergo a sharp transition from the EHM to the FI phase as Δ_F is varied across $\Delta_{F,c}$ by changing the drive amplitude. This sharp transition is depicted schematically by the dark red arrow in Fig. 1C (note that increasing $\Delta_{F,c}$ also decreases the value of κ, as it increases the density of states for phonon-assisted interband relaxation).

The physical difference between the EHM and FI phases is manifested in the response of the system to density perturbations. For demonstration, we numerically compute the density response to potential charge fluctuations, described by $\chi(q, \omega)$ (see Eq. 18). We examine the behavior of $\chi(q, \omega)$ as a function of driving amplitude

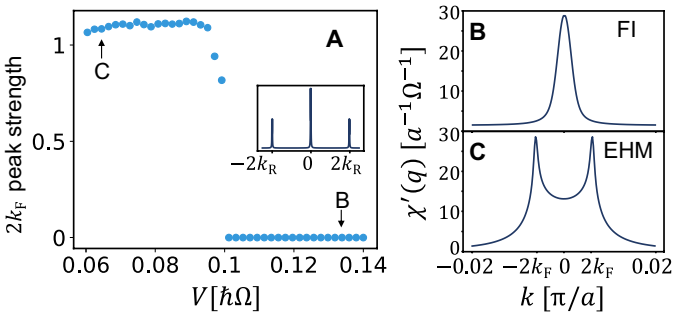

Fig. 4. Response of the steady state to density fluctuations. (**A**) Strength of the $2k_F$ peak, $\mathcal{F}$, as a function of the driving amplitude, V, across the critical value $V_c = 0.1\hbar\Omega$, corresponding to $\Delta_F = \Delta_{F,c}$. Inset: Full Fourier spectrum of the real part of the response function at zero frequency, $\chi'(q)$. (**B** and **C**) Zoom in on the Fourier peak of $\chi'(q)$ near $q = 0$. In the EHM phase (C), the Fourier transform exhibits $2k_F$ peaks, whereas in the FI phase (B), the function is smooth.

in the vicinity of the EHM-to-FI transition. For details of the numerical simulations, see section S3. The inset to Fig. 4A shows the real part of the response function $\chi'(q) = \mathrm{Re}[\chi(q, 0)]$. In the FI phase, $\chi(q)$ exhibits large peaks at zero wave number and at wave numbers connecting the two valleys at k_R and $-k_R$. Because of the sharp Fermi surface in the EHM phase, each peak splits into two peaks separated by $2k_F \equiv \pi n$. In particular, $\chi'(q)$ exhibits two peaks at $q = \pm 2k_F$. The splitting of these peaks is absent in the FI phase (see Fig. 4B and C). Experimental signatures of the split peaks are Friedel oscillations in the screening potential, which can be observed, for example, using x-ray scattering (*60*) and scanning tunneling microscopy (*61*–*63*) or through a minimally invasive electrostatic probe as in (*64*). In Fig. 4A, we plot the "strength" of the $2k_F$ peaks, defined as $\mathcal{F} = \frac{\chi'(2k_F)-\chi'(0)}{\chi'(0)}$, as a function of the driving field strength, V (i.e., along the trajectory depicted by the dark red arrow in Fig. 1C). The peaks disappear abruptly when the driving field imposes $\Delta_F > \Delta_{F,c}$, for which the steady state is in the FI phase.

DISCUSSION

To appreciate the physical scales, we estimate the value of κ in periodically driven semiconductors in the FI and EHM phases. To this end, we use a typical value for the radiative recombination lifetime, $\tau_{rr} \sim 1$ to 10 ns, and use the hot-electron lifetime as a typical time scale for phonon-mediated relaxation, $\tau_{he} \sim 10$ to 100 fs, respectively (*65*–*69*). We further take $k_R \sim 0.01\pi/a$. In the FI phase, this yields the estimate $\kappa a^2 \approx \frac{k_R a \tau_{he}}{\pi \tau_{rr}} \sim 10^{-6} - 10^{-8}$. In the EHM phase, the interband relaxation rate is suppressed by a factor $q_*^2 a^2 \sim \kappa a^2$ due to the small matrix element between the initial and final states (see Eq. 10). Therefore, for the EHM phase, we estimate $\kappa a^2 \approx \sqrt{\frac{k_R a}{\pi}\frac{\tau_{he}}{\tau_{rr}}} \sim 10^{-3} - 10^{-4}$. The low excitation density regime, where Eqs. 13 and 15 are valid, requires $\kappa < \kappa_0 \equiv (\Delta_F D_0)^2$. We estimate $D_0 = (\sqrt{2}\,\pi\hbar\, v_R)^{-1}$, where v_R is the band velocity of the semiconductor at the resonance momentum, k_R. In the EHM phase, the highest possible κ_0 is obtained for $\Delta_F \approx \Delta_{F,c} \equiv 2\hbar k_R v_s$ (see discussion in the second paragraph below Eq. 9). We thus estimate $\kappa_0 a^2 \approx 2(m_* v_s a/\pi\hbar)^2$, where $m_* \equiv \hbar k_R / v_R$ is the effective mass of the semiconductor. Therefore, large sound velocities and effective masses are favorable for realization of the EHM phase.

In this work, we uncovered a transition between EHM and FI phases in a driven one-dimensional electronic system. Our results can be generalized to other one- and two-dimensional resonantly driven Floquet-Bloch systems. In two-dimensional systems, we expect that the system still supports EHM and FI phases that can be accessed via the drive strength. Studying the features of the transition in two-dimensional systems and possibilities for controlling their behavior by reservoir engineering is an important direction for future study.

MATERIALS AND METHODS

Evaluation of the intrinsic scattering rates

We have evaluated the intrinsic scattering rates, $W_\lambda^{(l)}(k\nu, k'\nu')$, appearing below Eq. 4, through Floquet Fermi's golden rule. The rates are given by

$$W_\lambda^{(l)}(k\nu, k'\nu') = \frac{2\pi}{\hbar}\left|\sum_m \langle \phi_{k'\nu'}^{m+l} \mid U_\lambda(k-k', \omega_l) \mid \phi_{k\nu}^{m}\rangle\right|^2 \rho_\lambda(k-k', \omega_l) \tag{16}$$

where $\hbar\omega_l \equiv \varepsilon_{k\nu} - \varepsilon_{k'\nu'} - l\hbar\Omega$. For the full derivation, see section S4.

Floquet-Lindhard function

The density response to potential charge fluctuations, $\chi(x, t)$, is evaluated by the Floquet-Lindhard function. Following the Kubo formula, we define $\chi(x, t)$ through the density-density response function averaged over the driving period, $\mathcal{T} \equiv 2\pi/\Omega$

$$\chi(x,t) = \frac{\Theta(t)}{i\hbar\mathcal{T}}\int_0^{\mathcal{T}} d\tau \mathrm{Tr}\{\hat{\varrho}_{st}(t)\,[\hat{n}(x,t+\tau), \hat{n}(0,\tau)]\} \tag{17}$$

Here, $\Theta(t) = 1$ for $t > 0$ and $\Theta(t) = 0$; otherwise, $\hat{\varrho}_{st}$ is the steady-state density matrix and $\hat{n}(x) = \hat{\boldsymbol{c}}_x^\dagger \hat{\boldsymbol{c}}_x$ is the density operator, with $\hat{\boldsymbol{c}}_x = \int \frac{dk}{2\pi} e^{ikx} \hat{\boldsymbol{c}}_k$. We use $\hat{\varrho}_{st}(t) = \prod_{k\nu} [f_{k\nu} \hat{\phi}_{k\nu}^\dagger(t) \hat{\phi}_{k\nu}(t) + (1 - f_{k\nu}) \hat{\phi}_{k\nu}(t) \hat{\phi}_{k\nu}^\dagger(t)]$ to obtain the Floquet-Lindhard function (*70*)

$$\chi(q,\omega) = \sum_{\nu\nu' l}\int \frac{dk}{2\pi} \frac{\mathcal{M}_{\nu\nu'}^{(l)}(k, k-q)\,(f_{k-q\nu'} - f_{k\nu})}{\hbar\omega + \varepsilon_{k-q\nu'} - \varepsilon_{k\nu} - l\hbar\Omega + i0^+} \tag{18}$$

where $\mathcal{M}_{\nu\nu'}^{(l)}(k,k') = |\sum_m \langle \phi_{k\nu}^m | \phi_{k'\nu'}^{m-l}\rangle|^2$. For the full derivation, see (*71*).

SUPPLEMENTARY MATERIALS

Supplementary material for this article is available at http://advances.sciencemag.org/cgi/content/full/6/35/eaay4922/DC1

REFERENCES AND NOTES

1. T. Kitagawa, E. Berg, M. Rudner, E. Demler, Topological characterization of periodically driven quantum systems. *Phys. Rev. B* **82**, 235114 (2010).
2. Y. H. Wang, H. Steinberg, P. Jarillo-Herrero, N. Gedik, Observation of Floquet-Bloch states on the surface of a topological insulator. *Science* **342**, 453–457 (2013).
3. M. S. Rudner, N. H. Lindner, E. Berg, M. Levin, Anomalous edge states and the bulk-edge correspondence for periodically driven two-dimensional systems. *Phys. Rev. X* **3**, 031005 (2013).
4. M. C. Rechtsman, J. M. Zeuner, Y. Plotnik, Y. Lumer, D. Podolsky, F. Dreisow, S. Nolte, M. Segev, A. Szameit, Photonic Floquet topological insulators. *Nature* **496**, 196–200 (2013).
5. G. Jotzu, M. Messer, R. Desbuquois, M. Lebrat, T. Uehlinger, D. Greif, T. Esslinger, Experimental realization of the topological Haldane model with ultracold fermions. *Nature* **515**, 237–240 (2014).

6. A. G. Grushin, Á. Gómez-León, T. Neupert, Floquet fractional chern insulators. *Phys. Rev. Lett.* **112**, 156801 (2014).
7. F. Mahmood, C.-K. Chan, Z. Alpichshev, D. Gardner, Y. Lee, P. A. Lee, N. Gedik, Selective scattering between Floquet–Bloch and Volkov states in a topological insulator. *Nat. Phys.* **12**, 306–310 (2016).
8. P. Titum, E. Berg, M. S. Rudner, G. Refael, N. H. Lindner, Anomalous Floquet-Anderson insulator as a nonadiabatic quantized charge pump. *Phys. Rev. X* **6**, 021013 (2016).
9. F. Nathan, M. S. Rudner, N. H. Lindner, E. Berg, G. Refael, Quantized magnetization density in periodically driven systems. *Phys. Rev. Lett.* **119**, 186801 (2017).
10. L. J. Maczewsky, J. M. Zeuner, S. Nolte, A. Szameit, Observation of photonic anomalous Floquet topological insulators. *Nat. Commun.* **8**, 13756 (2017).
11. I. Martin, G. Refael, B. Halperin, Topological frequency conversion in strongly driven quantum systems. *Phys. Rev. X* **7**, 041008 (2017).
12. T. Oka, S. Kitamura, Floquet engineering of quantum materials. *Annu. Rev. Condens. Matter Phys.* **10**, 387–408 (2019).
13. A. V. Kimel, A. Kirilyuk, P. A. Usachev, R. V. Pisarev, A. M. Balbashov, T. Rasing, Ultrafast non-thermal control of magnetization by instantaneous photomagnetic pulses. *Nature* **435**, 655–657 (2005).
14. M. S. Rudner, N. H. Lindner, Band structure engineering and non-equilibrium dynamics in Floquet topological insulators. *Nat. Rev. Phys.* **2**, 229–244 (2020).
15. W. Yao, A. H. MacDonald, Q. Niu, Optical control of topological quantum transport in semiconductors. *Phys. Rev. Lett.* **99**, 047401 (2007).
16. T. Oka, H. Aoki, Photovoltaic Hall effect in graphene. *Phys. Rev. B* **79**, 081406 (2009).
17. A. Kirilyuk, A. V. Kimel, T. Rasing, Ultrafast optical manipulation of magnetic order. *Rev. Mod. Phys.* **82**, 2731–2784 (2010).
18. D. Fausti, R. I. Tobey, N. Dean, S. Kaiser, A. Dienst, M. C. Hoffmann, S. Pyon, T. Takayama, H. Takagi, A. Cavalleri, Light-induced superconductivity in a stripe-ordered cuprate. *Science* **331**, 189–191 (2011).
19. N. H. Lindner, G. Refael, V. Galitski, Floquet topological insulator in semiconductor quantum wells. *Nat. Phys.* **7**, 490 (2011).
20. N. H. Lindner, D. L. Bergman, G. Refael, V. Galitski, Topological Floquet spectrum in three dimensions via a two-photon resonance. *Phys. Rev. B* **87**, 235131 (2013).
21. Y. T. Katan, D. Podolsky, Modulated Floquet topological insulators. *Phys. Rev. Lett.* **110**, 016802 (2013).
22. J. Cayssol, B. Dóra, F. Simon, R. Moessner, Floquet topological insulators. *Phys. Status Solidi* **7**, 101–108 (2013).
23. W. Hu, S. Kaiser, D. Nicoletti, C. R. Hunt, I. Gierz, M. C. Hoffmann, M. Le Tacon, T. Loew, B. Keimer, A. Cavalleri, Optically enhanced coherent transport in $YBa_2Cu_3O_{6.5}$ by ultrafast redistribution of interlayer coupling. *Nat. Mater.* **13**, 705–711 (2014).
24. G. Goldstein, C. Aron, C. Chamon, Photoinduced superconductivity in semiconductors. *Phys. Rev. B* **91**, 054517 (2015).
25. M. Mitrano, A. Cantaluppi, D. Nicoletti, S. Kaiser, A. Perucchi, S. Lupi, P. Di Pietro, D. Pontiroli, M. Riccò, S. R. Clark, D. Jaksch, A. Cavalleri, Possible light-induced superconductivity in K_3C_{60} at high temperature. *Nature* **530**, 461–464 (2016).
26. A. Ghazaryan, T. Graß, M. J. Gullans, P. Ghaemi, M. Hafezi, Light-induced fractional quantum Hall phases in graphene. *Phys. Rev. Lett.* **119**, 247403 (2017).
27. A. Cavalleri, Photo-induced superconductivity. *Contemp. Phys.* **59**, 31–46 (2018).
28. S. Porta, L. Privitera, N. T. Ziani, M. Sassetti, F. Cavaliere, B. Trauzettel, Feasible model for photoinduced interband pairing. *Phys. Rev. B* **100**, 024513 (2019).
29. T. Ozawa, H. M. Price, A. Amo, N. Goldman, M. Hafezi, L. Lu, M. C. Rechtsman, D. Schuster, J. Simon, O. Zilberberg, I. Carusotto, Topological photonics. *Rev. Mod. Phys.* **91**, 015006 (2019).
30. Z. Gu, H. A. Fertig, D. P. Arovas, A. Auerbach, Floquet spectrum and transport through an irradiated graphene ribbon. *Phys. Rev. Lett.* **107**, 216601 (2011).
31. T. Kitagawa, T. Oka, A. Brataas, L. Fu, E. Demler, Transport properties of nonequilibrium systems under the application of light: Photoinduced quantum Hall insulators without Landau levels. *Phys. Rev. B* **84**, 235108 (2011).
32. L. D'Alessio, M. Rigol, Long-time behavior of isolated periodically driven interacting lattice systems. *Phys. Rev. X* **4**, 041048 (2014).
33. T. Iadecola, D. Campbell, C. Chamon, C.-Y. Hou, R. Jackiw, S.-Y. Pi, S. V. Kusminskiy, Materials design from nonequilibrium steady states: Driven graphene as a tunable semiconductor with topological properties. *Phys. Rev. Lett.* **110**, 176603 (2013).
34. H. Dehghani, T. Oka, A. Mitra, Dissipative Floquet topological systems. *Phys. Rev. B* **90**, 195429 (2014).
35. H. Dehghani, T. Oka, A. Mitra, Out-of-equilibrium electrons and the Hall conductance of a Floquet topological insulator. *Phys. Rev. B* **91**, 155422 (2015).
36. T. Iadecola, C. Chamon, Floquet systems coupled to particle reservoirs. *Phys. Rev. B* **91**, 184301 (2015).
37. T. Iadecola, T. Neupert, C. Chamon, Occupation of topological Floquet bands in open systems. *Phys. Rev. B* **91**, 235133 (2015).
38. T. Shirai, T. Mori, S. Miyashita, Condition for emergence of the Floquet-Gibbs state in periodically driven open systems. *Phys. Rev. E* **91**, 030101 (2015).
39. D. E. Liu, Classification of the Floquet statistical distribution for time-periodic open systems. *Phys. Rev. B* **91**, 144301 (2015).
40. H. Dehghani, A. Mitra, Occupation probabilities and current densities of bulk and edge states of a Floquet topological insulator. *Phys. Rev. B* **93**, 205437 (2016).
41. D. V. Else, B. Bauer, C. Nayak, Floquet time crystals. *Phys. Rev. Lett.* **117**, 090402 (2016).
42. V. Khemani, A. Lazarides, R. Moessner, S. Sondhi, Phase structure of driven quantum systems. *Phys. Rev. Lett.* **116**, 250401 (2016).
43. N. Yao, A. Potter, I.-D. Potirniche, A. Vishwanath, Discrete time crystals: Rigidity, criticality, and realizations. *Phys. Rev. Lett.* **118**, 030401 (2017).
44. S. Choi, J. Choi, R. Landig, G. Kucsko, H. Zhou, J. Isoya, F. Jelezko, S. Onoda, H. Sumiya, V. Khemani, C. von Keyserlingk, N. Y. Yao, E. Demler, M. D. Lukin, Observation of discrete time-crystalline order in a disordered dipolar many-body system. *Nature* **543**, 221–225 (2017).
45. J. Zhang, P. W. Hess, A. Kyprianidis, P. Becker, A. Lee, J. Smith, G. Pagano, I.-D. Potirniche, A. C. Potter, A. Vishwanath, N. Y. Yao, C. Monroe, Observation of a discrete time crystal. *Nature* **543**, 217–220 (2017).
46. I. Esin, M. S. Rudner, G. Refael, N. H. Lindner, Quantized transport and steady states of Floquet topological insulators. *Phys. Rev. B* **97**, 245401 (2018).
47. J. W. McIver, B. Schulte, F. U. Stein, T. Matsuyama, G. Jotzu, G. Meier, A. Cavalleri, Light-induced anomalous Hall effect in graphene. *Nat. Phys.* **16**, 38–41 (2020).
48. L. I. Glazman, Resonant excitation of carriers in a semiconductor by a high-power light pulse. *Zh. Eksp. Teor. Fiz.* **80**, 349 (1981).
49. L. I. Glazman, Kinetics of electrons and holes in direct-gap semiconductors photoexcited by high-intensity pulses. *Fiz. Tekh. Poluprovodn.* **17**, 790 (1983).
50. K. I. Seetharam, C.-E. Bardyn, N. H. Lindner, M. S. Rudner, G. Refael, Controlled population of Floquet-Bloch states via coupling to Bose and Fermi baths. *Phys. Rev. X* **5**, 041050 (2015).
51. K. I. Seetharam, C.-E. Bardyn, N. H. Lindner, M. S. Rudner, G. Refael, Steady states of interacting Floquet insulators. *Phys. Rev. B* **99**, 014307 (2019).
52. M. I. Dykman, M. Marthaler, V. Peano, Quantum heating of a parametrically modulated oscillator: Spectral signatures. *Phys. Rev. A* **83**, 052115 (2011).
53. E. O. Kane, Energy band structure in p-type germanium and silicon. *J. Phys. Chem. Solids* **1**, 82–99 (1956).
54. E. O. Kane, Band structure of indium antimonide. *J. Phys. Chem. Solids* **1**, 249–261 (1957).
55. C. L. Kane, E. J. Mele, Size, shape, and low energy electronic structure of carbon nanotubes. *Phys. Rev. Lett.* **78**, 1932–1935 (1997).
56. R. Egger, A. Zazunov, A. L. Yeyati, Helical Luttinger liquid in topological insulator nanowires. *Phys. Rev. Lett.* **105**, 136403 (2010).
57. K. Dorn, A. De Martino, R. Egger, Phase diagram and phonon-induced backscattering in topological insulator nanowires. *Phys. Rev. B* **101**, 045402 (2020).
58. H. Suzuura, T. Ando, Phonons and electron-phonon scattering in carbon nanotubes. *Phys. Rev. B* **65**, 235412 (2002).
59. V. M. Galitskii, S. P. Goreslavskii, V. F. Elesin, Z. Eksp, Electric and magnetic properties of a semiconductor in the field of a strong electromagnetic wave. *Teor. Fiz.* **57**, 207 (1969).
60. S. Rouzière, S. Ravy, J. P. Pouget, S. Brazovskii, Friedel oscillations and charge-density wave pinning in quasi-one-dimensional conductors: An x-ray diffraction study. *Phys. Rev. B* **62**, R16231 (2000).
61. M. C. van der Wielen, A. J. van Roij, H. van Kempen, Direct observation of Friedel oscillations around incorporated Si_{Ga} dopants in GaAs by low-temperature scanning tunneling microscopy. *Phys. Rev. Lett.* **76**, 1075–1078 (1996).
62. L. Petersen, P. Sprunger, P. Hofmann, E. Lægsgaard, B. Briner, M. Doering, H. Rust, A. Bradshaw, F. Besenbacher, E. Plummer, Direct imaging of the two-dimensional Fermi contour: Fourier-transform STM. *Phys. Rev. B* **57**, R6858 (1998).
63. K. Kanisawa, M. J. Butcher, H. Yamaguchi, Y. Hirayama, Imaging of Friedel oscillation patterns of two-dimensionally accumulated electrons at epitaxially grown InAs(111) A surfaces. *Phys. Rev. Lett.* **86**, 3384–3387 (2001).
64. I. Shapir, A. Hamo, S. Pecker, C. P. Moca, Ö. Legeza, G. Zarand, S. Ilani, Imaging the electronic Wigner crystal in one dimension. *Science* **364**, 870–875 (2019).
65. C. A. Schmuttenmaer, C. C. Miller, J. W. Herman, J. Cao, D. A. Mantell, Y. Gao, R. J. D. Miller, Femtosecond time-resolved photoemission study of hot electron relaxation at the GaAs(100) surface. *Chem. Phys.* **205**, 91–108 (1996).
66. S. K. Sundaram, E. Mazur, Inducing and probing non-thermal transitions in semiconductors using femtosecond laser pulses. *Nat. Mater.* **1**, 217–224 (2002).
67. P. Avouris, M. Freitag, V. Perebeinos, Carbon-nanotube photonics and optoelectronics. *Nat. Photonics* **2**, 341–350 (2008).
68. Y. Arafat, F. M. Mohammedy, M. M. Shahidul Hassan, Optical and Other Measurement Techniques of Carrier Lifetime in Semiconductors. *Int. J. Optoelectron. Eng.* **2**, 5 (2012).
69. X. Li, K. Zhang, F. Toor, J. Treu, L. Stampfer, G. Koblmueller, J. P. Prineas, Radiative and Nonradiative Recombination Coefficients of InAs/InAlAs Core-shell Nanowires. in *2018 Conf. Lasers Electro-Optics* (2018), pp. 1–2.
70. M. Torres, A. Kunold, Kubo formula for Floquet states and photoconductivity oscillations in a two-dimensional electron gas. *Phys. Rev. B* **71**, 115313 (2005).
71. M. S. Rudner, N. H. Lindner, The Floquet engineer's handbook. arXiv:2003.08252 [cond-mat.mes-hall] (18 March 2020).

Acknowledgments: We would like to thank T. Gulden, G. K. Gupta, V. Kalnitsky, G. Matsman, and A. Turner for discussions and D. Cohen and Y. Katz for technical support. **Funding:** N.H.L. acknowledges support from the European Research Council (ERC) under the European Union Horizon 2020 Research and Innovation Programme (grant agreement no. 639172) and from the Israeli Center of Research Excellence (I-CORE) "Circle of Light." M.S.R. acknowledges the support of the European Research Council (ERC) under the European Union Horizon 2020 Research and Innovation Programme (grant agreement no. 678862) and the Villum Foundation. I.E. acknowledges support from the Ministry of Science and Technology, Israel. **Author contributions:** I.E. performed the numerical and analytic calculations. All authors contributed to the data analysis and wrote the manuscript. **Competing interests:** The authors declare that they have no competing interests. **Data and materials availability:** All data needed to evaluate the conclusions in the paper are present in the paper and/or the Supplementary Materials. Additional data related to this paper may be requested from the authors.

Submitted 1 July 2019
Accepted 13 July 2020
Published 26 August 2020
10.1126/sciadv.aay4922

Citation: I. Esin, M. S. Rudner, N. H. Lindner, Floquet metal-to-insulator phase transitions in semiconductor nanowires. *Sci. Adv.* **6**, eaay4922 (2020).

Floquet metal-to-insulator phase transitions in semiconductor nanowires

Iliya Esin, Mark S. Rudner and Netanel H. Lindner

Sci Adv **6** (35), eaay4922.
DOI: 10.1126/sciadv.aay4922